AIAA JOURNAL
Vol. 48, No. 1, January 2010

Computations of Flapping Flow Propulsion for Unmanned Underwater Vehicle Design

Ravi Ramamurti,* Jason Geder,† John Palmisano,‡ and Banahalli Ratna§
U.S. Naval Research Laboratory, Washington, D.C. 20375-5344
and
William C. Sandberg¶
Science Applications International Corporation, McLean, Virginia 22102

DOI: 10.2514/1.43389

Three-dimensional unsteady computations of the flow past a flapping and deforming fin are performed. The computed unsteady lift and thrust force–time histories are validated with experimental data and are in good agreement. Several fin parametric studies are performed for a notional unmanned underwater vehicle. The parametric studies investigated the force production of the fin as a function of varying the flexibility, the bulk amplitude of fin rotation, the vehicle speed, and the fin stroke bias angle. The results of these simulations are used to evaluate the hydrodynamic performance of the vehicle and to support controller development. Computations are also performed to map out the hydrodynamic characteristics of a new test vehicle, designed and built at Naval Research Laboratory to demonstrate the hovering and low-speed maneuvering performance of a set of actively controlled curvature fins.

I. Introduction

UNMANNED underwater vehicles (UUVs) have demonstrated their capabilities in applications including inspection, surveillance, exploration, and object detection. These capabilities are of considerable value, particularly in environments that are dangerous or impossible for a human to navigate. Current technology has allowed UUVs to excel at tasks including deep-sea diving, high-speed motion, and long-distance traversal. The low-speed, high-maneuverability operations required of many near-shore and littoral-zone missions present different mobility challenges that may require different solutions.

Flapping fins are an attractive alternative to thrusters for overcoming the difficulties associated with low-speed maneuverability in the presence of ocean currents and near-shore obstacles. Aquatic animals certainly achieve high levels of controllability at near-zero forward speed. Blake [1] determined that in low-speed operations labriform motion (using pectoral-fin oscillation) is more efficient for maneuvering than carangiform motion (using body and caudal-fin undulation). This result suggests that a flapping pectoral fin can be mounted on a rigid UUV hull without sacrificing low-speed maneuverability. Many investigators have studied fin propulsion both theoretically and experimentally. There have been several comprehensive surveys published summarizing the history in this field, such as those by Platzer and Jones [2], Rozhdestvensky and Ryzhov [3], and Shyy et al. [4]. Many experimental investigations have also been carried out to study the performance of oscillating surfaces as propulsors installed in unmanned underwater vehicles. Kato et al. [5] and Ando et al. [6] have developed and incorporated both lift-based and drag-based deformable pectoral fins into unmanned underwater vehicles. Tangorra et al. [7] have developed a flapping fin based on the bluegill sunfish for use as a propulsor. They have used computational fluid dynamics (CFD) simulations and proper orthogonal decomposition analysis to identify the first few modes of measured fin deformation that produce the majority of the force. This has enabled them to avoid trying to replicate the entire measured fin-deformation time history. None of these previous flapping fin propulsor investigations have, however, provided the capability to initially predict the precise temporal surface curvature variation needed to create a specified mission force–time history. One of the distinguishing features of our research is that we have computed the deforming fin force–time histories first, as a function of fin surface curvature variation, to achieve a desired vehicle hovering and maneuvering performance. Our deforming fin was subsequently developed with the active deformation needed to produce that surface curvature time variation.

Walker and Westneat [8] have studied the fin kinematics of a class of lift-based labriform fish, the bird wrasse (*Gomphosus varius*), whose force production is a good match with our performance objectives. Ramamurti et al. [9] computationally studied the force production of the bird wrasse and achieved good agreement with Walker and Westneat [8]. The computational method used to study the force production of the bird wrasse has been applied to the design and development of an actively controlled-curvature biomimetic pectoral fin by Palmisano et al. [10]. The resulting actuated fin design has been built and incorporated into a prototype test vehicle for demonstrating its dynamic performance in propulsion and low-speed maneuvering.

We have chosen a two-fin test vehicle design in order to demonstrate deforming fin force production with vertical plane and yaw control in an underwater environment, using a simple vehicle configuration. The primary objectives of the current study are to select the shape of the fin that allows flexibility while keeping the mechanical system less complex. In-water laboratory experiments of the standalone fin to obtain deformation time history and the associated fin force production time history have already been carried out, and those results are described below. The computational results using an unstructured grid-based Navier-Stokes solver feflo are validated against this experimental data. Three-dimensional unsteady computations of a notional unmanned underwater vehicle with flapping fins are also carried out. Several parametric studies varying the amplitude

Presented as Paper 724 at the AIAA 47th Aerospace Sciences Meeting, Orlando, FL, 5–8 January 2009; received 22 January 2009; revision received 4 August 2009; accepted for publication 4 August 2009. This material is declared a work of the U.S. Government and is not subject to copyright protection in the United States. Copies of this paper may be made for personal or internal use, on condition that the copier pay the $10.00 per-copy fee to the Copyright Clearance Center, Inc., 222 Rosewood Drive, Danvers, MA 01923; include the code 0001-1452/10 and $10.00 in correspondence with the CCC.

*Aerospace Engineer, Laboratory for Computational Physics and Fluid Dynamics; ravi@lcp.nrl.navy.mil. Associate Fellow AIAA.

†Aerospace Engineer, Laboratory for Computational Physics and Fluid Dynamics; jgeder@lcp.nrl.navy.mil.

‡Roboticist, Center for Bio-Molecular Science and Engineering; palmisano@gmail.com.

§Director, Center for Bio-Molecular Science and Engineering; banahalli.ratna@nrl.navy.mil.

¶Senior Scientist, Analysis and Modeling Division; william.c.sandberg@saic.com. Senior Member AIAA.

and frequency of oscillation of the fin, the flexibility of the fin, and the stroke bias angle are performed. The objective of these computations is to create force–time histories for a range of operating conditions of the vehicle. The results of the computations are used to map the forces to kinematics. This mapping will be used for controller development and to evaluate vehicle performance.

II. Incompressible Flow Solver

The governing equations employed are the incompressible Navier-Stokes equations in arbitrary Lagrangian–Eulerian (ALE) formulation, which are written as

$$\frac{\mathrm{d}\mathbf{v}}{\mathrm{d}t} + \mathbf{v}_a \cdot \nabla\mathbf{v} + \nabla p = \nu\nabla^2\mathbf{v} \tag{1}$$

$$\nabla \cdot \mathbf{v} = 0 \tag{2}$$

where p denotes the pressure, ν is the kinematic viscosity, $\mathbf{v}_a = \mathbf{v} - \mathbf{w}$ is the advective velocity vector, $\mathbf{v}$ is the flow velocity, and $\mathbf{w}$ is the mesh velocity, and the material derivative is with respect to the mesh velocity $\mathbf{w}$. Both the pressure p and the viscous stress tensor have been normalized by the (constant) density ρ and are discretized in time using an implicit time-stepping procedure. Thus, the equations are Eulerian for zero mesh velocity and Lagrangian if the mesh velocity is the same as the flow velocity. The present time-accurate flow solver is discretized in space using a Galerkin procedure with linear tetrahedral elements. The details of the flow solver have already been discussed extensively elsewhere (Ramamurti et al. [11,12]), in connection with successfully validated solutions for numerous two-dimensional and three-dimensional, laminar and turbulent, and steady and unsteady flow problems.

III. Results and Discussion

Ramamurti and Sandberg [13] have computed the unsteady flow past a UUV with flapping fins. They have studied the effect of varying the amplitude and frequency of oscillation of the fin and the angle of attack at the root of the fin. They have found the near-optimum parameters for enabling the vehicle to hover in a 3 kt (1.543 m/s) current to be a fin root angle of attack of 20° (α_r), a fin flapping frequency of 2 Hz, and a fin stroke amplitude of 114°. The angle of attack α_r in that study was the angle of the root of the fin chord with respect to the inflow direction, shown in Fig. 1. In the present effort, the feflo incompressible flow solver is used to compute the unsteady three-dimensional flow past an isolated flapping fin at hovering conditions, and is validated by comparisons with the in-water experimental data measured at the U.S. Naval Research Laboratory (NRL). Computations are performed to investigate the effects on force production by varying parameters such as vehicle speed, flapping frequency, flexibility of the fin, and starting location of the downstroke of the fin. The results of these simulations are coupled with the test vehicle hydrodynamic characteristics and incorporated into the development of the vehicle controller, so as to enable a stable and maneuverable UUV.

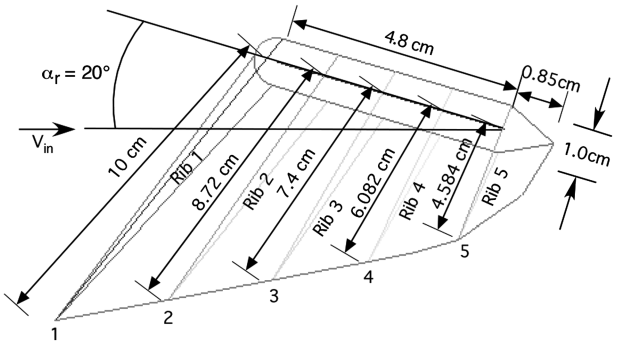

Fig. 1 Schematic of the deforming fin showing the root cross section and the five ribs.

A. Fin Design and Test Setup

Ramamurti et al.[14] have studied the effect of variable rigidity of the bird wrasse fin on the fluid dynamics of force production. Based on this study, we have reduced the number of ribs of the mechanical fin from 14 spines in the fish to 5 equally spaced ribs, in order to reduce the complexity of the mechanical system while maintaining enough flexibility of the fin surface to achieve the curvature computed to be necessary. An actively deforming mechanical fin has been designed, using compliant ribs and built by Palmisano et al. [10]. This experimental design and setup is shown in Fig. 2. The fin rib is a compliant structure, designed to bend to a specific base-to-tip deflection angle when subjected to translational forces at the base of the rib. The topology of the compliant ribs was designed using a structural optimization based on the synthesis approach of Trease et al. [15]. The fin is composed of five such ribs, each actuated by a single servo motor. The phasing of the actuators is specified in conjunction with the bulk rotation of the entire fin, in order to obtain the desired instantaneous shape throughout the stroke. In addition to the actuation of each individual rib, the bulk rotation of the fin throughout the flapping cycle is controlled by a servo motor. The entire set of five ribs is encased in a liquid silicone rubber skin, which is designed to elastically deform. A small water tank (76 cm× 30 cm × 46 cm) is used to test the actuation of the fin. In this initial setup, a torque cell and a load cell, coaxial with the bulk rotation axis, are used to measure the thrust, lift, and moment about the axis. To protect the expensive load and torque sensors, the fin rotation axis in the experiment is located at 1.3 cm above the water surface. This led to the drawback in the measurement setup that the fin surface is not fully submerged underwater.

The force measurement device is modified using a gantry, described by Palmisano et al. [16] and shown in Fig. 3, so that the fin is fully submerged underwater. Also, a pair of torque sensors placed orthogonal to each other replaces the coaxial load cell and the torque cells. One of the torque cells measures the fin thrust, while the second one measures the lift force and the moment. To derive the forces from the torque cell measurements, the spanwise location of the center of

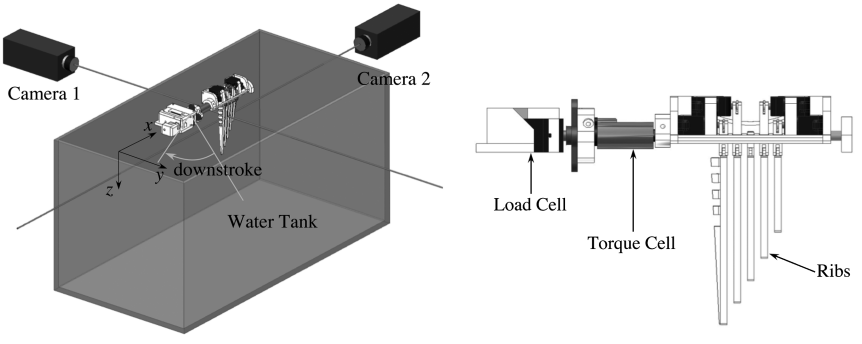

a) **b)**

Fig. 2 Experimental setup: a) tank and camera locations and b) side view of the fin and sensor locations.

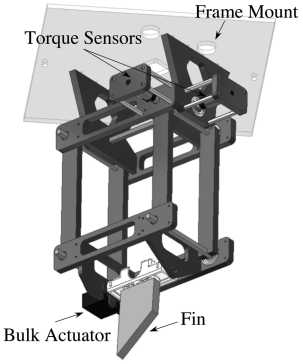

Fig. 3 Modified fin forces measuring device.

pressure on the fin is needed, in addition to the offset of the axis of fin rotation from the sensor axis and from the bulk rotation angle. The location of the center of pressure is obtained form the computations performed with the rigid fin, and it remains nearly constant at 0.06 m from the root of the fin.

The kinematics of the flapping fin are obtained using the two-high-speed-camera system shown in Fig. 2a and described by Geder et al. [17]. The two cameras are positioned nearly orthogonal to each other, in order to maximize the accuracy of the position measurements, because this arrangement provides the most unique field of view for each of the cameras. The set of two two-dimensional-camera pixel coordinates is then converted to a single set of three-dimensional-world coordinates. To calibrate this camera system, we must collect images of points with known three-dimensional location covering the space in which the fin will operate. For this purpose, a structure of LEGO bricks is devised and suspended in the field of interest. Sufficient points to cover the field of interest are marked on this structure, and both two-dimensional pixel coordinates from both cameras as well as the actual three-dimensional coordinates of the points are recorded. The tips of the five ribs of the fin described in the previous section are marked. Their location in space and time throughout the stroke will describe the kinematics of the fin tip.

In the computations, the deforming shape of the fin is constructed using a spline line passing through the tips of the ribs and the root of the rib, shown in Fig. 1. Therefore, the deforming shape of the fin is controlled by the prescribed motion of the tips of the ribs and does not include the fluid structure interaction on the surface of the fin. More precise kinematics of the deforming fin could be obtained if one were to use an array of markers distributed on both the surfaces of the fin, but this will involve additional camera systems, as all the markers will not be visible in a two-camera system at all instants during the flapping cycle, due to the opaque skin and also the variable thickness of the fin.

In the initial setup, in order to obtain the bulk rotation of the root of the fin, the angle by which the fin tip of the third rib is rotated about

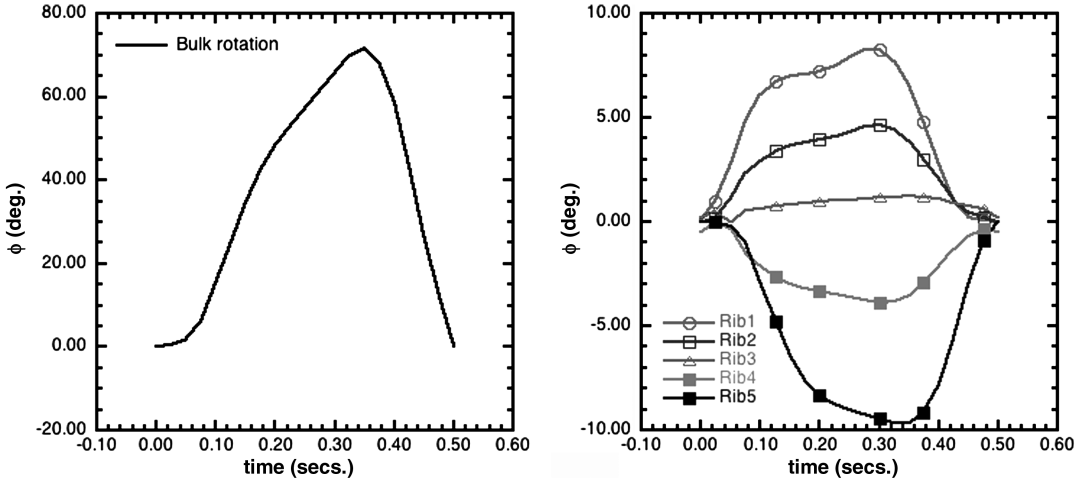

Fig. 4 Baseline kinematics for $f = 2.0$ Hz: a) bulk rotation and b) relative rib rotation.

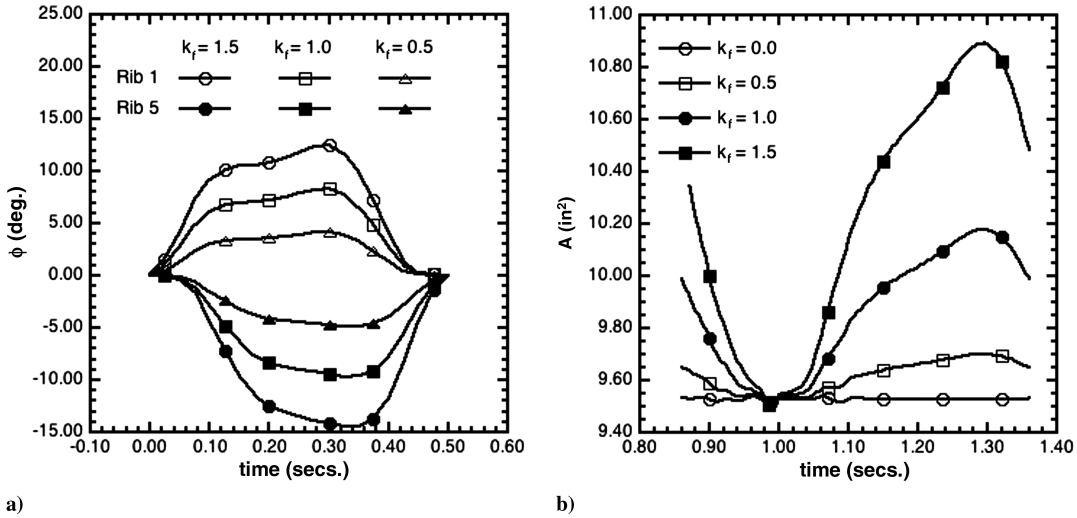

Fig. 5 Effect of controlled deformation on a) relative rotation of leading- and trailing-edge ribs and b) wetted surface area of the fin.

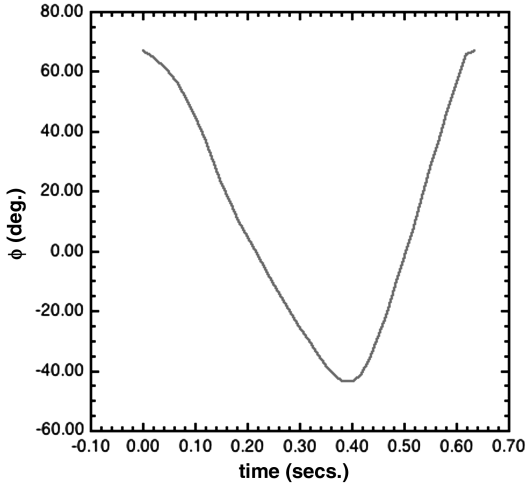

Fig. 6 Kinematics for a rigid fin flapping at 1.579 Hz.

the axis is used, because this rib is not actuated. However, high-speed videos of this initial setup showed that this rib does bend. Hence, in the new setup, an additional rigid marker rod was added downstream of the trailing edge to correctly measure the bulk rotation angle.

B. Baseline Kinematics

The deforming motion of the fin shown in Fig. 1 is obtained by prescribing the motion of the five control points or the tips of the rib (1–5). The kinematics of the ribs are decomposed into two motions. The first is a rotation of all the ribs about the fin axis of rotation, termed as the bulk rotation (Fig. 4a); the second is a supplemental rib rotation, which is crucial for obtaining the deforming shape of the fin (Fig. 4b). The combined motion can be written as

$$\phi_i(t) = k_b \phi_{\text{bulk}}(t) + k_f \phi_{\text{rel}(i)}(t) + \phi_0, \qquad i = 1, 5 \tag{3}$$

where k_b and k_f are factors that can be varied to achieve various bulk amplitudes and relative flexibility, respectively, and ϕ_0 is the starting position of the downstroke of the fin. These baseline kinematics that mimic the bird wrasse were used by Ramamurti and Sandberg [13] and in this paper in order to study the effect of bulk amplitude, deformation of the fin, and flapping frequency.

In this study, prescribing the five fin tip locations controls the deforming shape of the fin. The different relative rotations of each of the ribs give rise to the deforming shape of the fin throughout the stroke. Figure 5a shows the relative rotation of the leading- and trailing-edge ribs for three different deformation factors k_f. The maximum difference between the relative rotations between these two ribs increased from a value of 8.75° for $k_f = 0.5$ to 26.25° for $k_f = 1.5$. The variation of the wetted surface area of the fin throughout the stroke is shown in Fig. 5b, and it increases from a minimum of 9.5 in^2 for the rigid fin ($k_f = 0.0$) to a maximum of 10.9 in^2 for the fully flexible fin ($k_f = 1.5$).

C. Validation of CFD Results for a Rigid Fin

The force–time-history experimental data was obtained for a rigid fin by turning off the actuation of the individual ribs and retaining only the bulk rotation. The measured kinematics of the rigid flapping fin are shown in Fig. 6. The amplitude of the fin oscillation is 110.7°. The computed force–time history is shown in Fig. 7. The mean thrust obtained from the computation is 0.078 N and the mean lift during the cycle is −0.13 N. To obtain the lift and thrust forces from the experimental data, the mean moment arm is required. This was obtained by computing the center of pressure from the computations, shown in Fig. 7c. For the case of this rigid fin, the center of pressure remains nearly constant at 0.06 m. This value was used in deriving the forces from the experimental data. Figure 7b shows a good comparison of the computed lift with that of the experiments. The force transducer used in this setup was not able to capture the variation during the cycle, as the sensitivity of this transducer was nearly 0.13 N and the maximum variation in the thrust throughout the stroke is less that 0.2 N. Also, in this initial setup, to protect the expensive load and torque sensors from water damage, the fin rotation axis was located above the water surface. This resulted in indeterminable surface interactions, such as waves and air ingestion that covered part

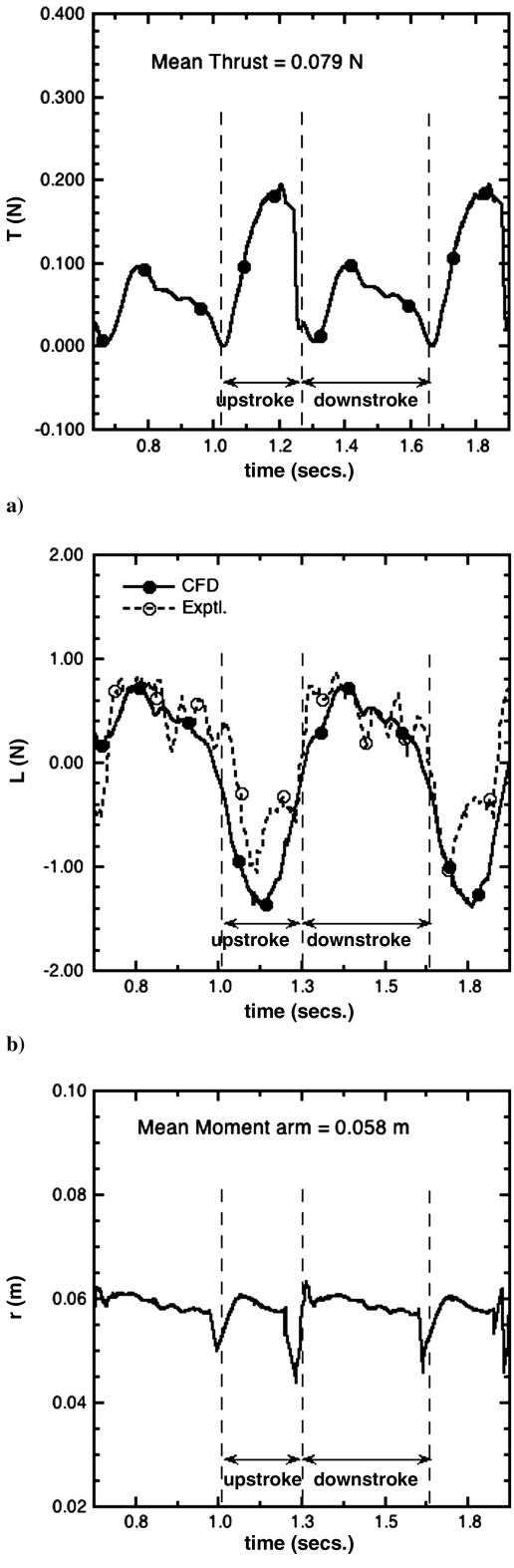

Fig. 7 Variation of a) thrust, b) lift, and c) mean center of pressure from a fin flapping at 1.579 Hz ($V = 0$ kt).

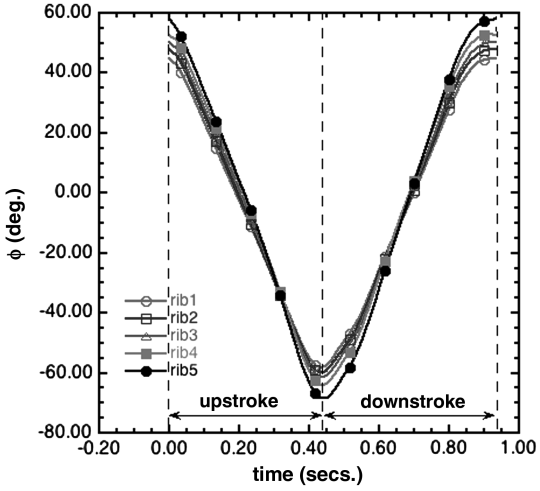

Fig. 8 Kinematics of a deforming fin ($f = 1.0715$ Hz and $V = 0$ kt).

of the root section of the fin. Hence, the experimental setup was modified using a gantry. This allowed the entire fin to be submerged in a larger tank while transferring the moments to the two crosswise-mounted torque sensors.

D. Validation for a Deforming Fin

With the improved experimental setup, a new set of kinematics was programmed into the rib actuator servos, shown in Fig. 8. This set yielded a bulk rotation amplitude of 111.6°, with the leading-edge rib having an amplitude of 103° and the trailing-edge rib having an amplitude of 126.5°. Although the amplitude of the ribs are opposite of that of the bird wrasse, where the amplitude of the leading edge is larger compared with the trailing edge, computations were performed with this set of kinematics. Also, for the fin flapping at 1.0715 Hz, the period of upstroke is 0.433 s, and the period of downstroke is 0.5 s. In contrast, the bird wrasse fin has a 1:2 ratio between the periods of upstrokes and downstrokes.

Figure 9 shows the comparison of the thrust and lift production between the CFD results and the experimental data. The comparison of the computed thrust–time history with the experimental results is very good. For the lift, the computed results compare reasonably well during the downstroke but do not capture the peaks during the upstroke. The mean thrust and lift produced in this case from the CFD results are 0.058 and 0.005 N, respectively. The corresponding mean thrust and lift forces from the experimental data are 0.059 and −0.052 N, respectively. Figure 10 shows the variation of the moment about the axis of rotation and the center of pressure on the fin from the computed results. Figure 10b shows that the moment arm varies between 0.045 and 0.065 m during the stroke, with the mean moment arm remaining nearly at 0.058 m.

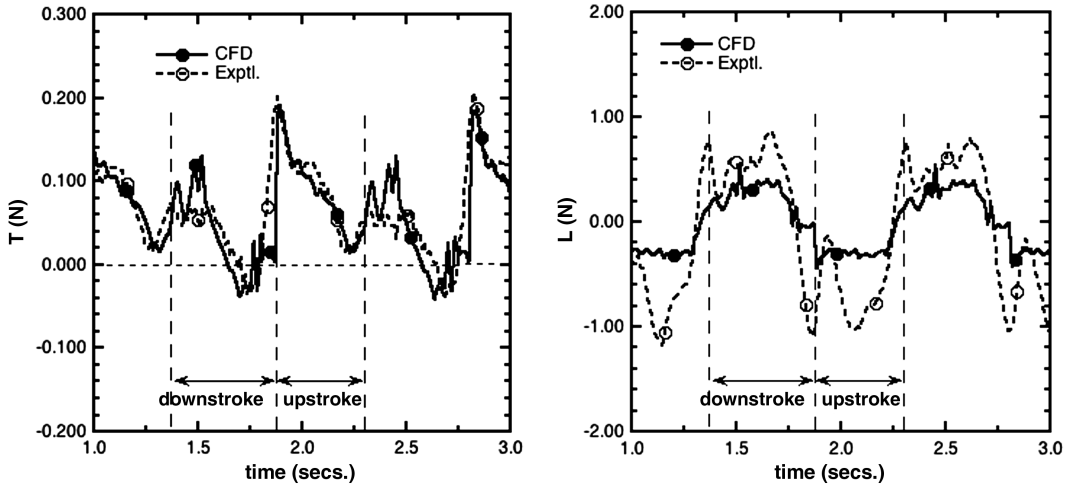

a) b)

Fig. 9 Comparison of force production for a deforming fin ($f = 1.0715$ Hz and $V = 0$ kt).

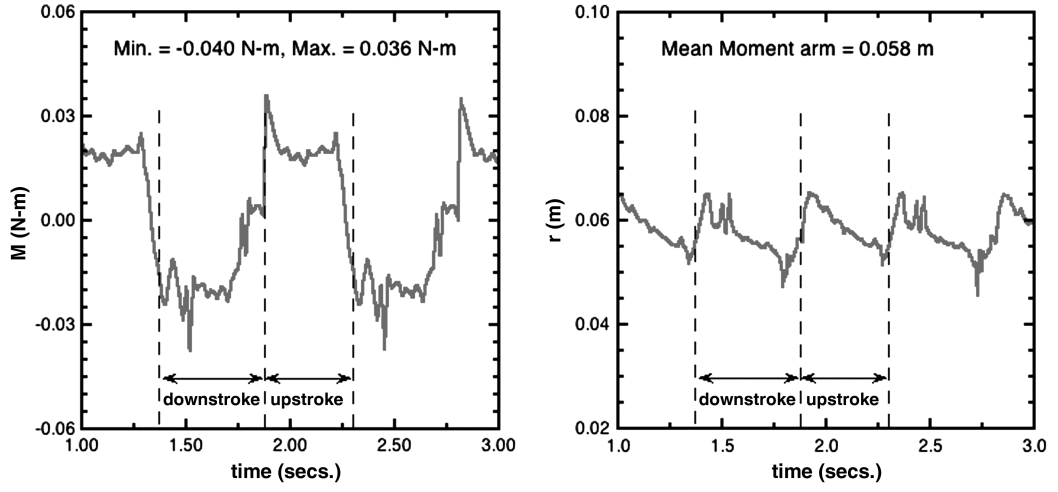

a) b)

Fig. 10 Results from a flapping deforming fin ($f = 1.0715$ Hz and $V = 0$ kt): a) moment about axis of rotation and b) center of pressure.

Figure 11 shows the velocity vector at a plane cut 0.0635 m from the root of the fin. At $t = 1.304$ s, just before the stroke reversal, we see the leading-edge vortex shed below the fin (Fig. 11a); after stroke reversal to downstroke, at $t = 1.4578$ s, the leading- and trailing-edge vortices are seen above the fin (Fig. 11b). Close to this instant, the thrust produced reaches a maximum. During the middle of the downstroke, $t = 1.706$ s, an attached leading-edge vortex is seen from Fig. 11c; at $t = 1.7037$ s (Fig. 11d), this vortex is elongated and detaches from the leading edge before $t = 1.8367$ s (Fig. 11e), where the thrust produced is a minimum during the downstroke. Just after stroke reversal into the upstroke, $t = 1.8999$ s (Fig. 11f), we can see both leading- and trailing-edge vortices formed, the trailing-edge vortex being shed into the wake (Fig. 11g) and the leading-edge vortex elongating as the upstroke proceeds. These results show the qualitative wake features during the flapping cycle. Extreme caution has to be applied if one has to use the wake measurements in order

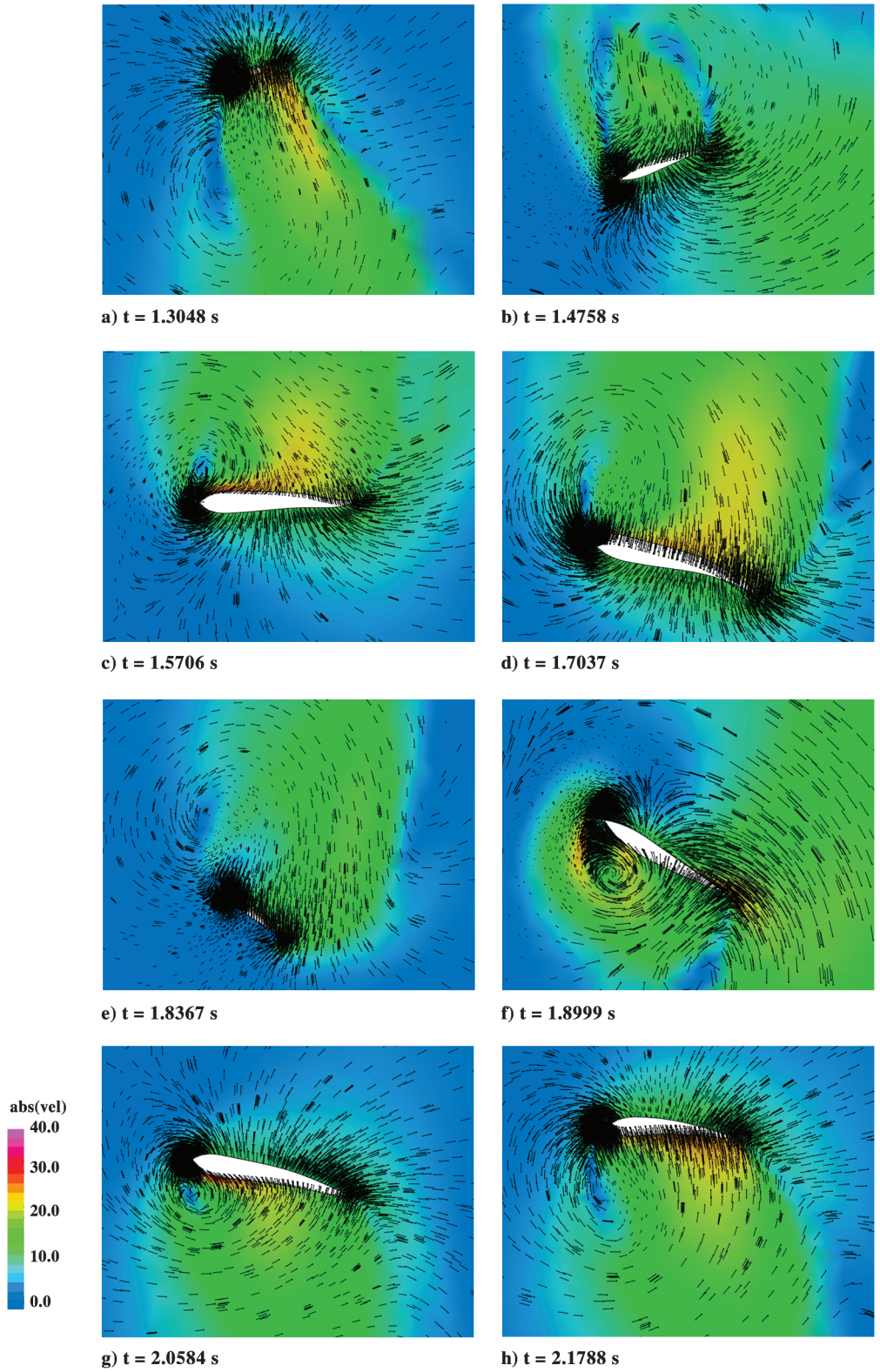

Fig. 11 Velocity vectors on a plane cut at $x = 0.0508$ m from the root of the fin, showing the evolution of the leading- and trailing-edge vortices during the a–e) downstroke and f–h) upstroke.

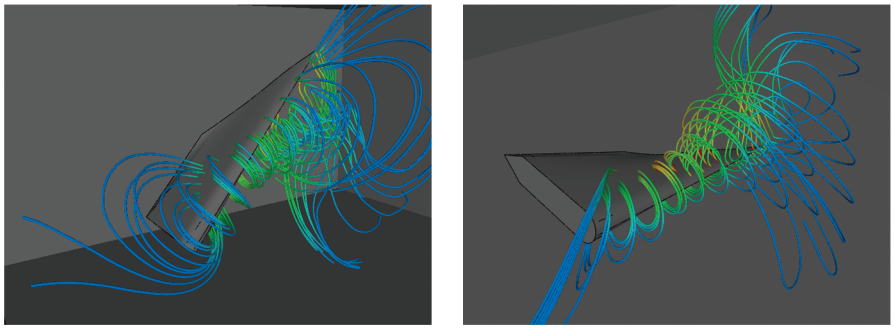

a) t = 1.3065 s b) t = 1.6713 s

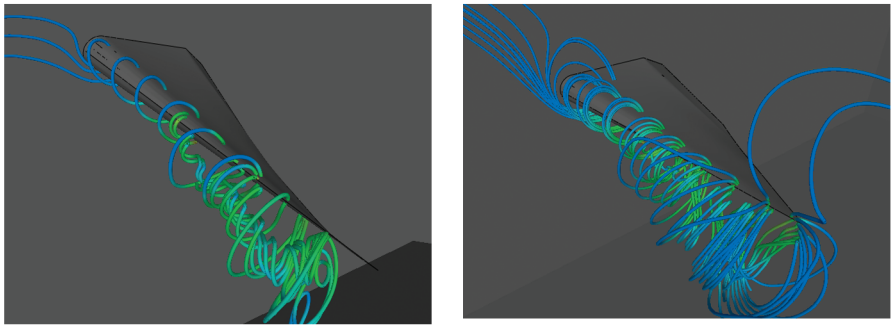

c) t = 1.9428 s d) t = 2.0575 s

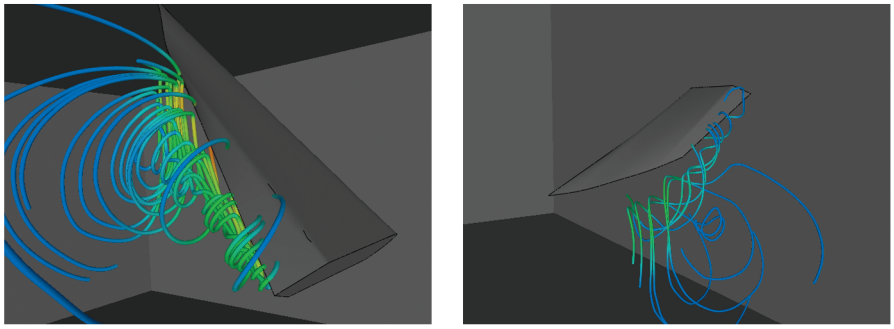

e) t = 1.3065 s f) t = 1.9428 s

Fig. 12 Instantaneous particle traces released from a rake a–d) in front of the leading edge and e–f) after the trailing edge.

to arrive at the forces produced by the flapping fin. Bohl and Koochesfahani [18] have recently shown that using only the mean velocity in the wake to obtain the forces leads to higher thrust coefficient compared with using the additional fluctuating components of the wake velocity. They have shown that, using the complete wake velocity, the experimental force coefficients match well with the CFD results of Ramamurti and Sandberg [19] for a two-dimensional oscillating NACA 0012 airfoil. Figure 12 shows the

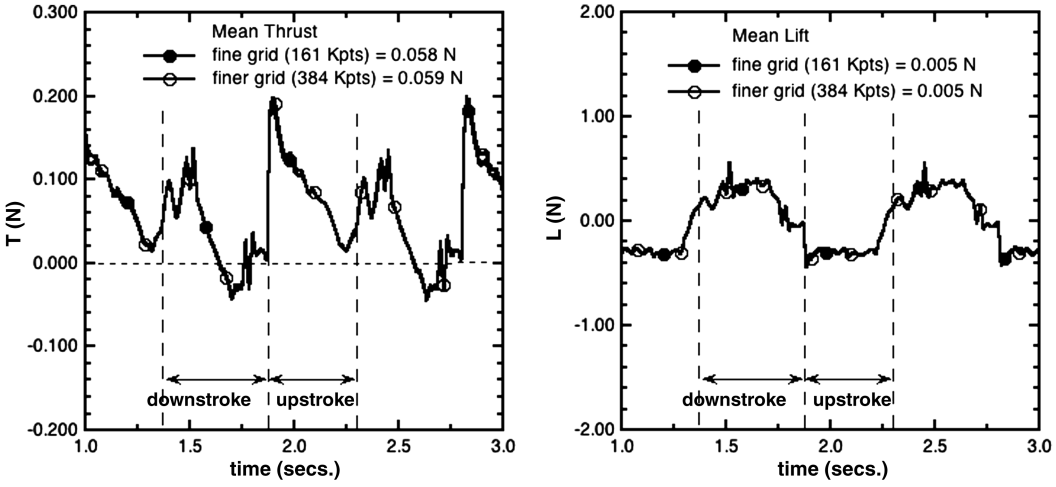

a) b)

Fig. 13 Effect of grid refinement on force production.

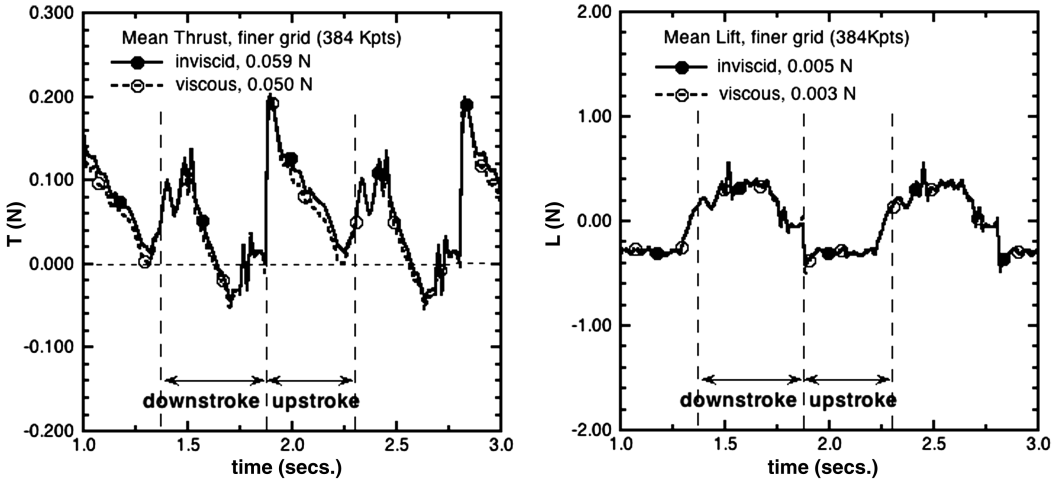

a) b)

Fig. 14 Effect of viscosity on force production.

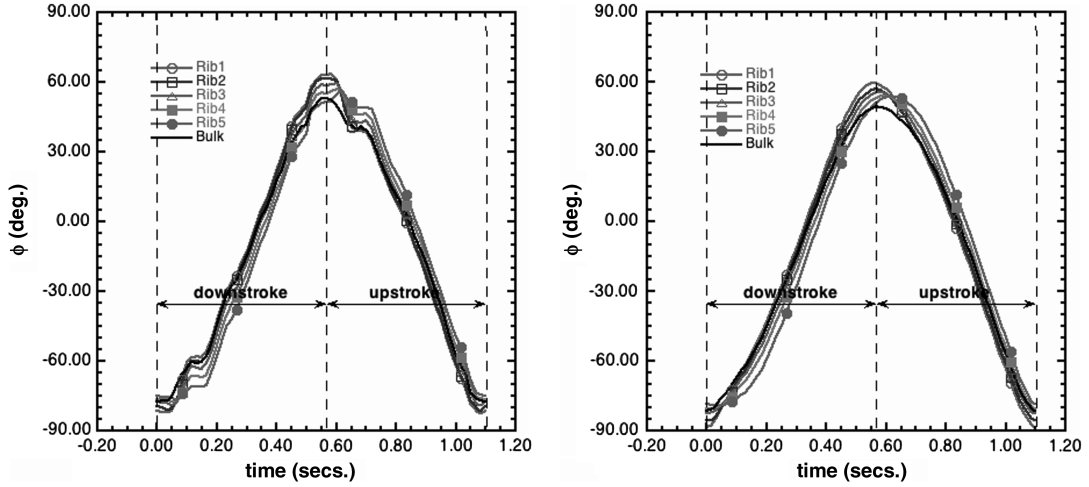

a) b)

Fig. 15 Kinematics for a flapping deforming fin from a) raw data and b) smoothed data ($f = 0.9091$ Hz).

instantaneous particle traces released from a rake just in front of the leading edge, Figs. 12a–12d, just before the stroke reversal into the downstroke, $t = 1.3065$ s, during the middownstroke, $t = 1.6713$ s, just after stroke reversal into the upstroke, $t = 1.9428$ s, and during the middle of the upstroke, $t = 2.0575$ s. These traces show the presence of the leading-edge vortex that detaches from the surface of the fin in the middle of the span. Also, the spanwise flow in the core of the vortex is seen to extend from the middle of the span to the wing tip

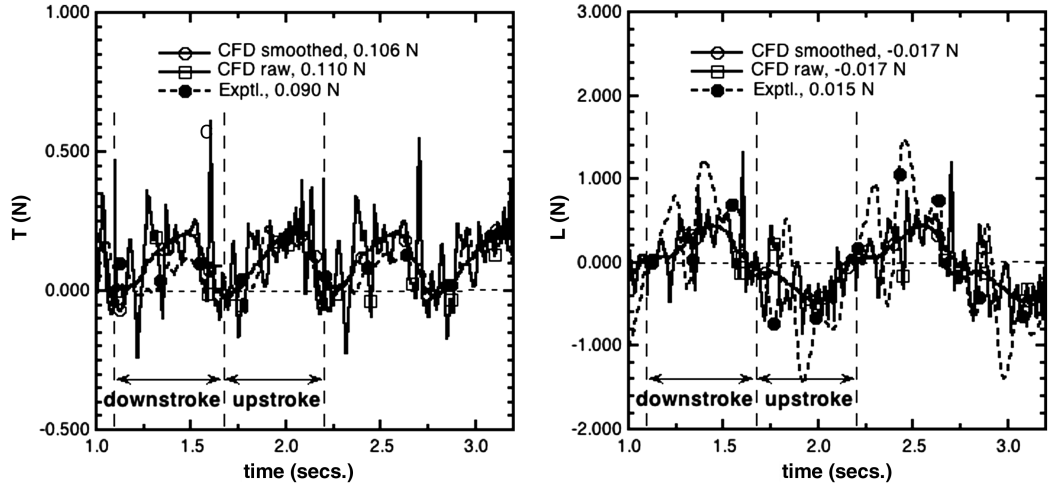

a) b)

Fig. 16 Comparison of force production for a deforming fin ($f = 0.9091$ Hz and $V = 0$ kt).

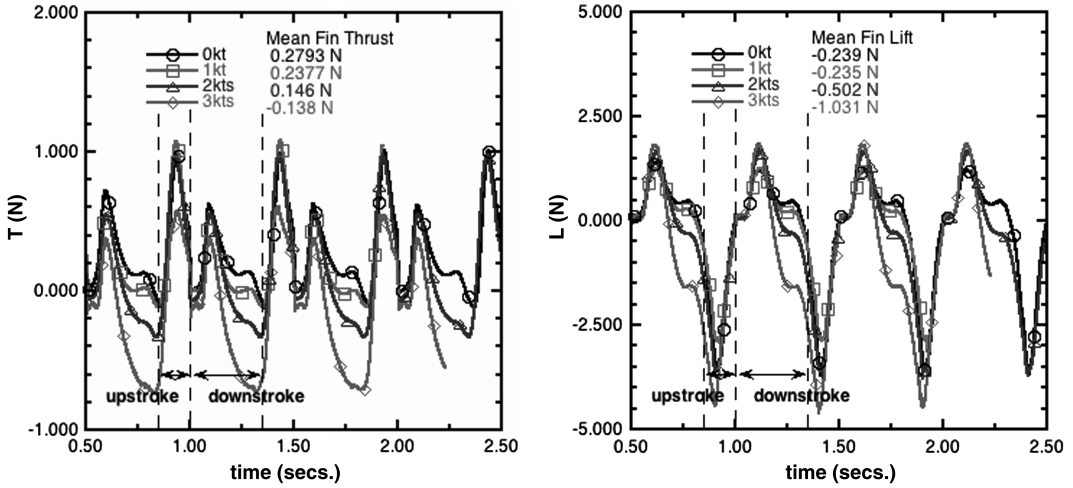

a) b)

Fig. 17 Effect of vehicle speed on thrust and lift production ($f = 2.0$ Hz and $k_f = 1.5$).

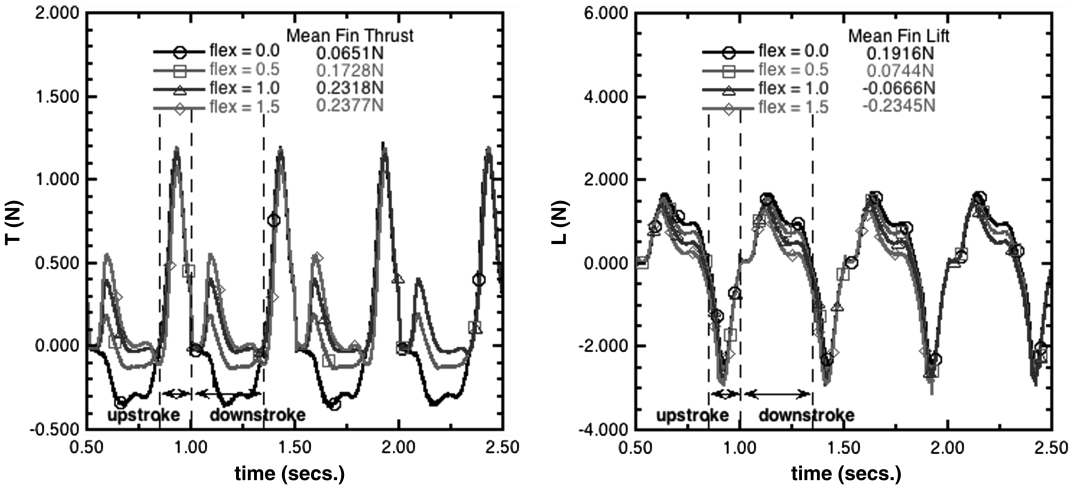

a) b)

Fig. 18 Effect of flexibility on thrust and lift production ($f = 2.0$ Hz and $V = 1$ kt).

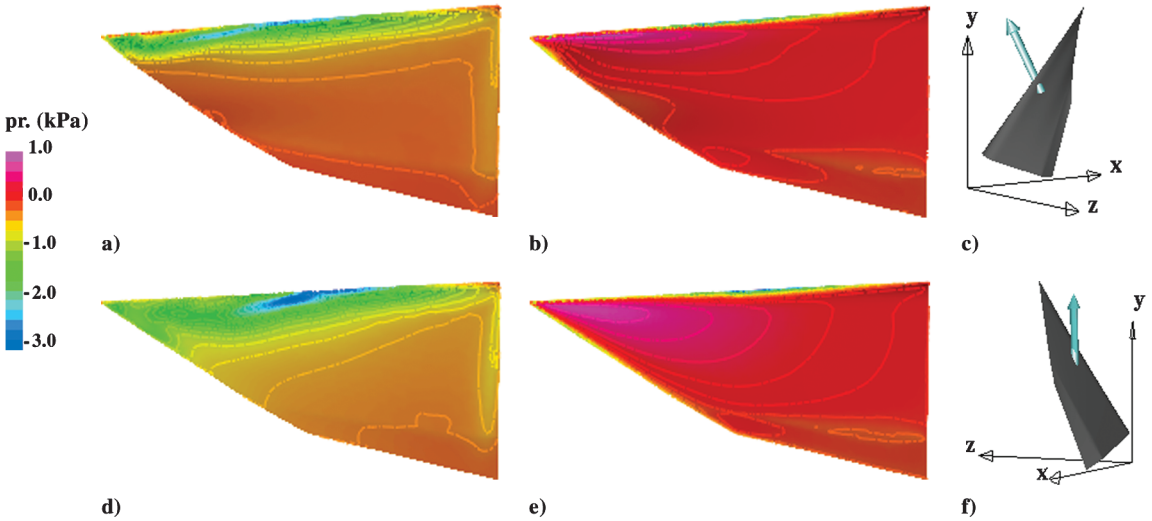

Fig. 19 Comparison of surface pressure distribution and force vector during downstroke: a–c) flexible fin and d–f) rigid fin ($t = 1.09$ s, $f = 2.0$ Hz, and $V = 1.0$ kt).

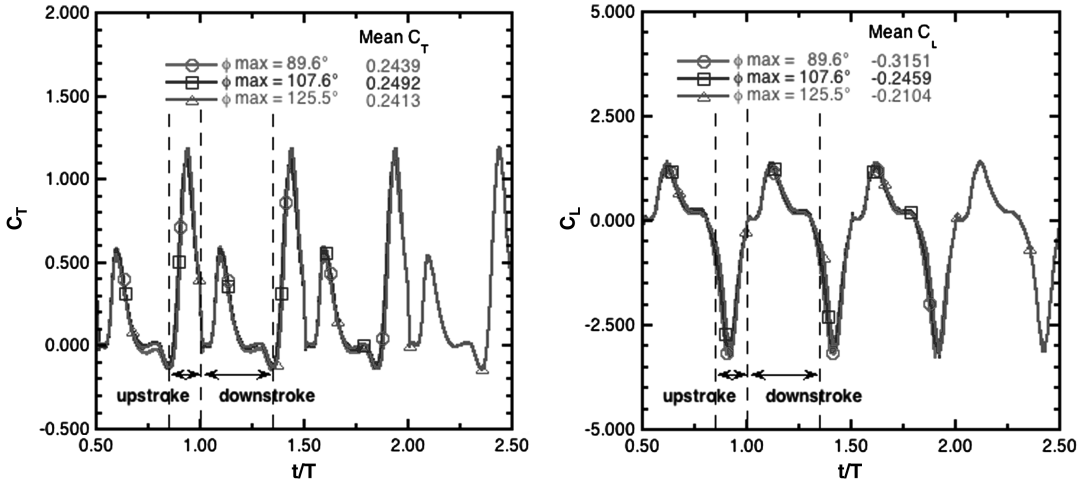

a) b)

Fig. 20 Time history of coefficients of thrust and lift for various bulk amplitudes ($f = 2.0$ Hz and $V = 1$ kt).

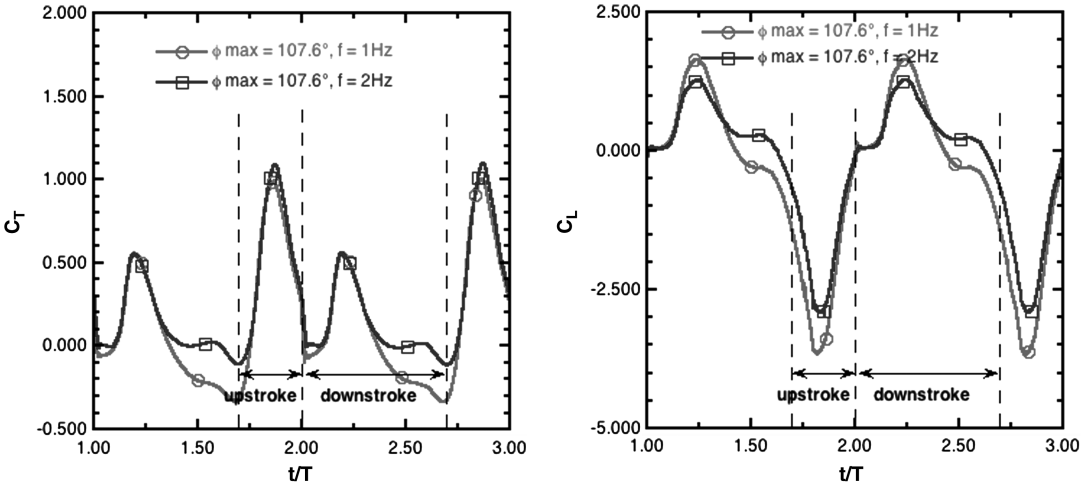

a) b)

Fig. 21 Effect of flapping frequency on thrust and lift coefficients ($V = 1$ kt).

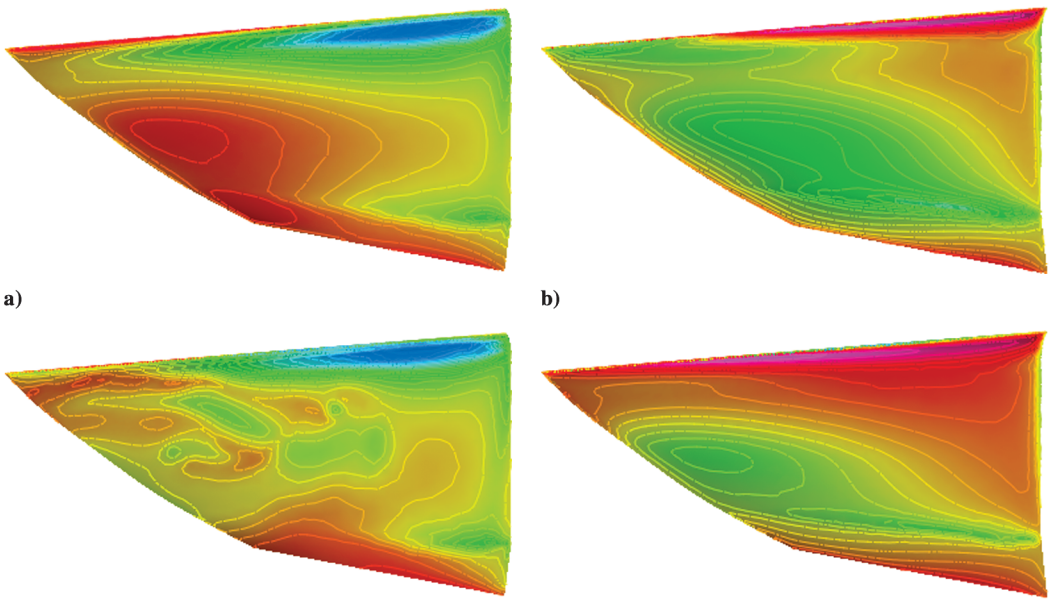

a) b)

c) d)

Fig. 22 Surface pressure distribution on the fin at $t/T = 2.5$: a–b) $f = 1$ Hz and c–d) $f = 2$ Hz.

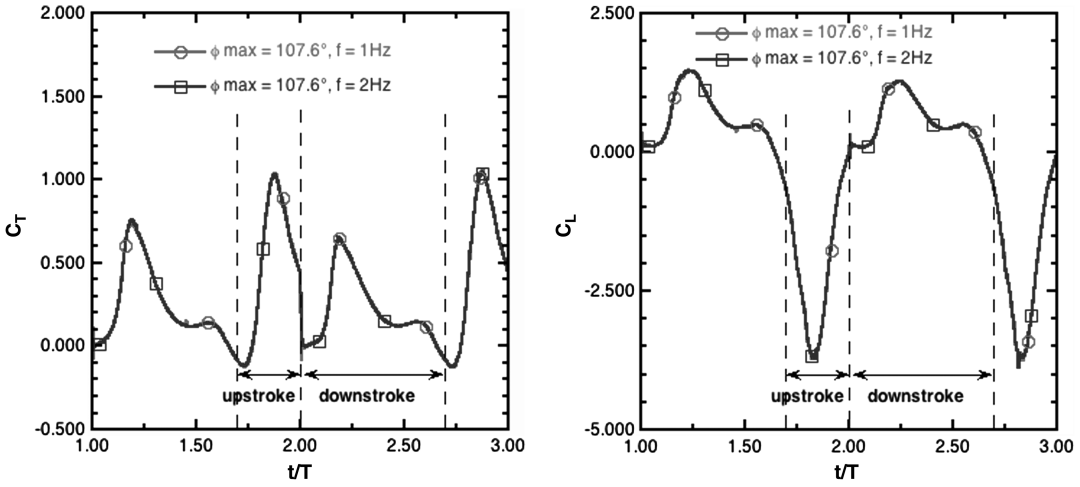

Fig. 23 Effect of flapping frequency on thrust and lift coefficients ($V = 0$ kt).

(Figs. 12c and 12d). Similar spanwise flow is also observed in the particle traces released from near the trailing edge just before the stroke reversal, $t = 1.3065$ s. The trailing-edge vortex that was shed after stroke reversal into the upstroke, $t = 1.428$ s, is also seen in Fig. 12f.

A grid-refinement study was conducted to assess the sensitivity of the computed results to spatial resolution. The mesh spacing near the fin was halved, and the total number of grid points in the computational domain increased from 161,000 points to 384,000 points. Figure 13 shows the effect of grid refinement on the force production. It is clear that the mesh with 161,000 points is sufficient. The effect of viscosity on the force production was investigated by carrying out the simulation that was performed with a finer mesh of 384,000 points and a Smagorinsky [20] turbulence model. The Reynolds number Re for the viscous computation was 13,400, based on mean tip speed $V_{\text{tip}} = 0.4175$ m/s and the mean chord of the fin $\bar{c} = 0.03205$ m. The results show that the effect of viscosity is minimal, Fig. 14. This confirms our earlier findings on flapping insect wings (Ramamurti and Sandberg [21]) and fish fins (Ramamurti et al. [9]), that the force production is inertially dominated due to large-amplitude flapping motion.

To understand the differences in the lift production during the upstroke, another set of kinematics that mimics the bird wrasse was programmed into the servos for the ribs. The bulk rotation angle was measured using the additional marker rod instead of using rib 3. The experimental kinematics are shown in Fig. 15a. They were smoothed based on the acceleration of the tips of the ribs, resulting in the kinematics shown in Fig. 15b. The amplitude of the bulk rotation of the fin 130°, the amplitude of the leading-edge rib is 147° and that of the trailing edge is 131.3°. Although the upstroke is slower than the desired bird wrasse kinematics, the phasing of the individual ribs and the amplitude are closer to it.

With this set of kinematics, the computed results were compared to the experimentally obtained thrust and lift, shown in Fig. 16. The computed results using the raw and the smoothed kinematics envelop the force–time history obtained experimentally, and the agreement is good in terms of thrust. The experimental lift curves still exhibit peaks outside the CFD envelope. The reason for this could be the use of a constant moment arm, in the case of deforming fin for the data reduction. Another reason for the differences is that, in the experiments, the surface of the fin deforms due to the fluid structure interaction, which is not modeled in the computations. In the remainder of the study, the computations are performed based on idealized baseline kinematics obtained from the bird wrasse kinematics and other varying pertinent controllable parameters.

E. Parametric Studies

The controllable fin parameters that were varied in this study are the bulk amplitude, relative deformability of the fin, flapping fin frequency, starting position of the downstroke, and vehicle speed. Simulations were performed across all these parameters, and the results are summarized below.

First, we summarize the effect of vehicle speed on the thrust and lift generation of a fin flapping at 2 Hz. For this simulation, k_b and k_f were set to 1.5, and $\phi_0 = -85°$. Figure 17 shows the variation of thrust and lift production for vehicle speeds ranging from hovering to 3 kt. As the vehicle speed is increased, the mean thrust produced decreases. The flapping fin is able to provide positive thrust up to 2 kt. The mean lift also decreases with increase in vehicle speed, Fig. 17b,

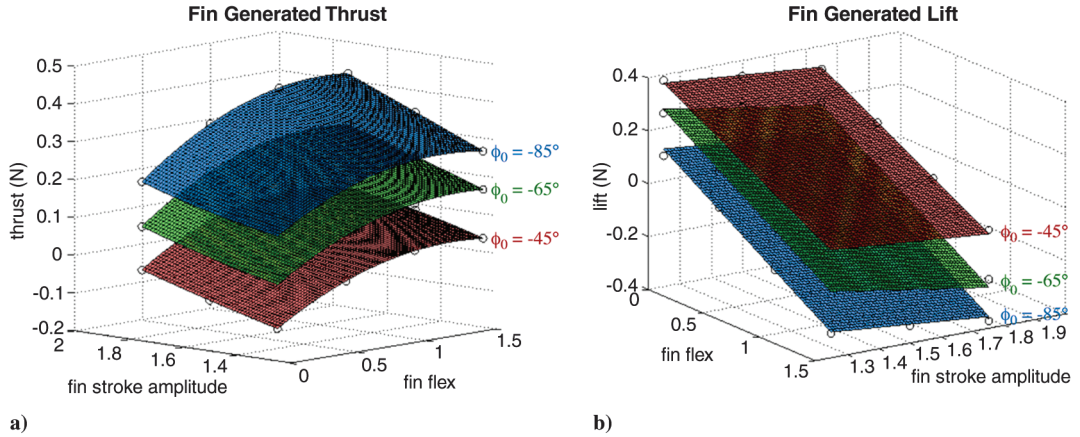

Fig. 24 Mean thrust and lift forces generated by the flapping fin ($f = 2.0$ Hz and $V = 1.0$ kt).

and the lift excursion also increases, especially during the upstroke. This suggests that modification of the fin kinematics is necessary, if we wish to operate above 2 kt (1.029 m/s). Since we are primarily interested in the 0–2 kt range, we have not pursued this yet. Next, the flexibility of the fin was varied from a rigid fin ($k_f = 0.0$) to a fully flexible fin ($k_f = 1.5$). For this test, the vehicle speed of 1 kt (0.5144 m/s) and a flapping frequency of 1 Hz were maintained constant. As the fin is made more flexible, the mean thrust produced increases nearly four-fold (Fig. 18a) from a rigid fin (0.065 N) to a fully flexible fin (0.238 N). The rigid fin produces negative thrust or drag during the downstroke while the flexible fins produce positive thrust. This positive effect is offset by the loss of lift in the flexible fins (Fig. 18b). The surface pressure distribution on the top and bottom surfaces of the fin, at an instant when the thrust reaches a maximum during the downstroke ($t = 1.09$ s) for the flexible fin, is shown in Figs. 19a and 19b. The rigid fin at the same instant shows a much lower pressure on the top surface (Fig. 19d) and a higher pressure on the bottom surface (Fig. 19e) compared with that of the flexible fin. Figures 19c and 19f show the resultant force vector and the orientation of the fin at this instant. For clarity, the transverse component of the force vector is neglected and the vector is not drawn to scale in the figure. It is clear that the resultant force for the flexible fin is in the negative x direction but for the rigid fin is along the x-axis, yielding a drag force.

The effect of the amplitude of fin rotation was studied by choosing $k_b = \{1.25, \quad 1.5, \quad 1.75\}$. This resulted in a bulk amplitude of 89.6, 107.6, and 125.5°, respectively. For this study, a fully flexible fin, $k_f = 1.5$, was used, with a vehicle speed of 1 kt (0.5144 m/s) and a flapping frequency of 2 Hz maintained constant. As expected, as the amplitude increased, the mean lift decreased and thrust forces increased. The mean thrust increased from 0.1615 to 0.2377 N and achieved a maximum of 0.3132 N; the mean lift increased from −0.2087 to −0.2345 N and achieved a maximum of −0.2731 N. When the forces were normalized using

$$C_F = \frac{F}{\frac{1}{2}\rho V_{tip}^2 A_{fin}} \tag{4a}$$

where ρ is the density of water, R is the length of the leading-edge rib, f is the flapping frequency, A_{fin} is the average area of the fin during the stroke, and V_{tip} is the mean velocity of the fin tip defined by

$$V_{tip} = 2\phi_{bulk} R f \tag{4b}$$

the force–time history merges into one curve, as shown in Figs. 20a and 20b. Similar results are obtained by increasing the frequency of flapping from 1 to 2 Hz, as shown in Fig. 21. Although both the lift and thrust coefficients can be described reasonably well by a single curve during the upstroke of the flapping cycle, they are different during the downstroke of the cycle. This is due to the fact that although the pressure distribution on the bottom surface of the fin remains qualitatively similar (Figs. 22a and 22c), the pressure distribution for the 2 Hz case on the top surface of the fin exhibits lower pressure and unsteadiness (Fig. 22b). For a hovering vehicle, $V = 0$ kts, the coefficients of thrust and lift for the two frequencies studied collapse into a single curve, as shown in Figs. 23a and 23b. The purpose of computing the force coefficients in this research effort is to guide the controller design to properly interpolate between the various bulk amplitudes and the frequencies of interest and to not arrive at a universal force coefficient that encompasses all the parameters. To arrive at the proper scaling of the forces, the forward speed of the vehicle, i.e., an advance ratio with respect to the fin-tip speed, the angle of attack of the root of the fin with the incoming flow,

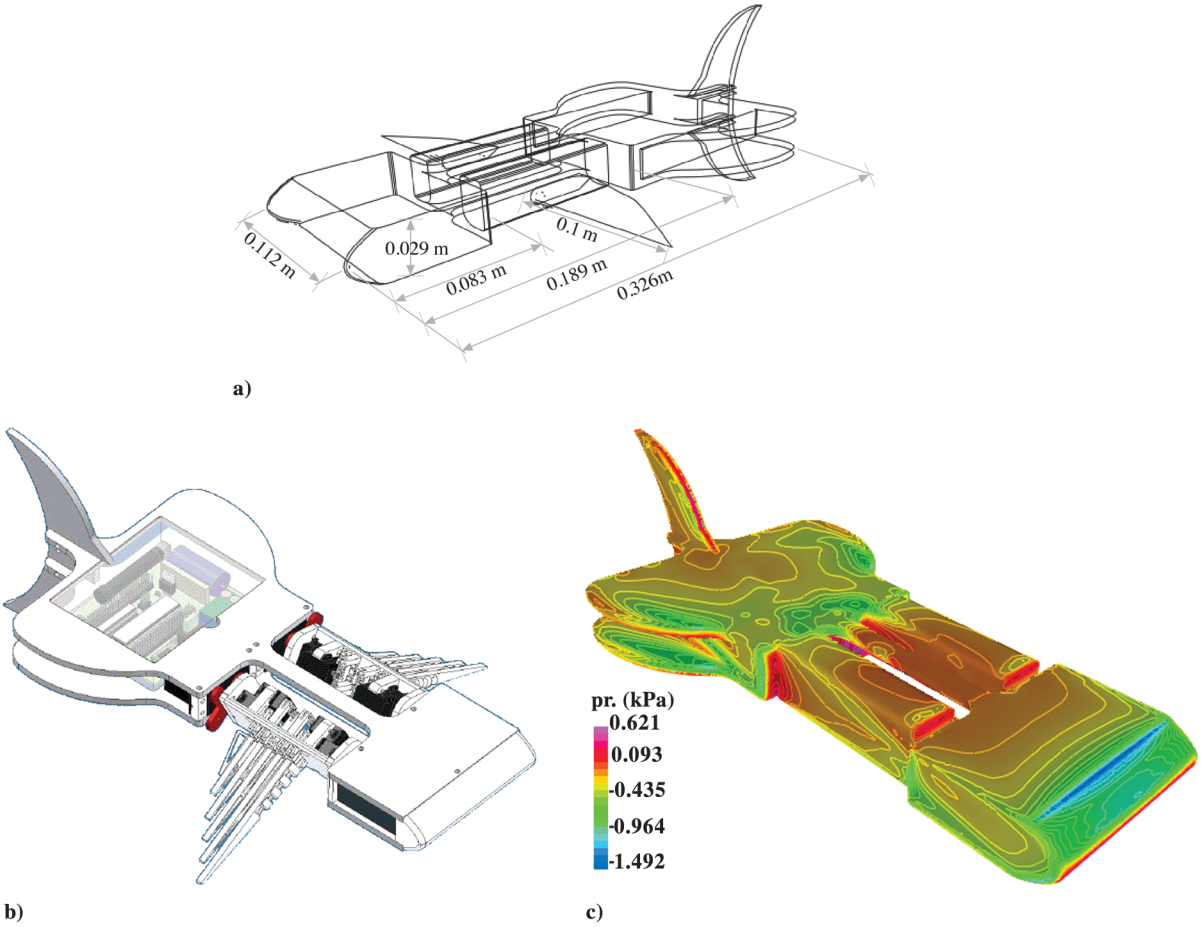

Fig. 25 NRL-UUV test Vehicle: a) Schematic of vehicle, b) vehicle carrying a set of two actively controlled curvature fins, and c) Surface pressure distribution on NRL-UUV swimming at 2 kt ($\alpha = 20°$ and $\beta = 0°$).

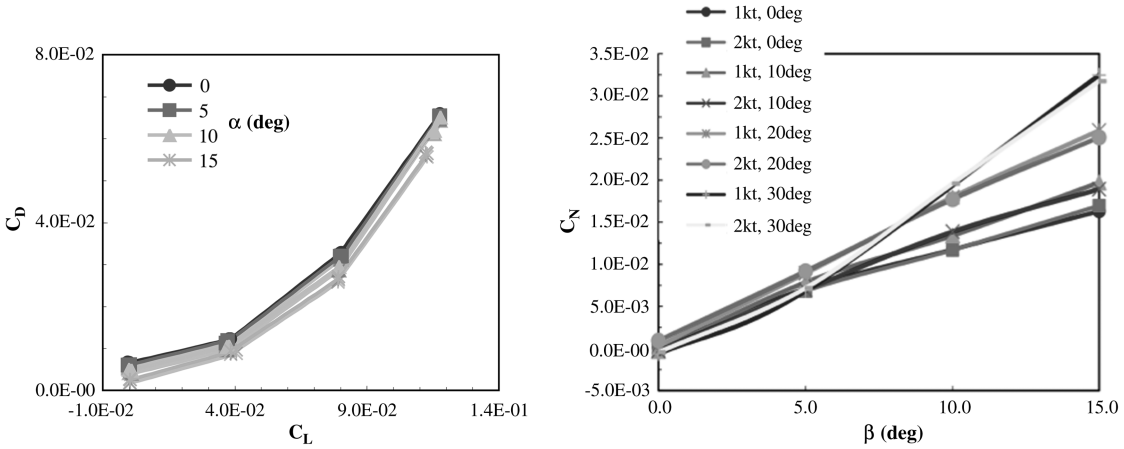

Fig. 26 Hydrodynamics characteristics of the NRL-UUV.

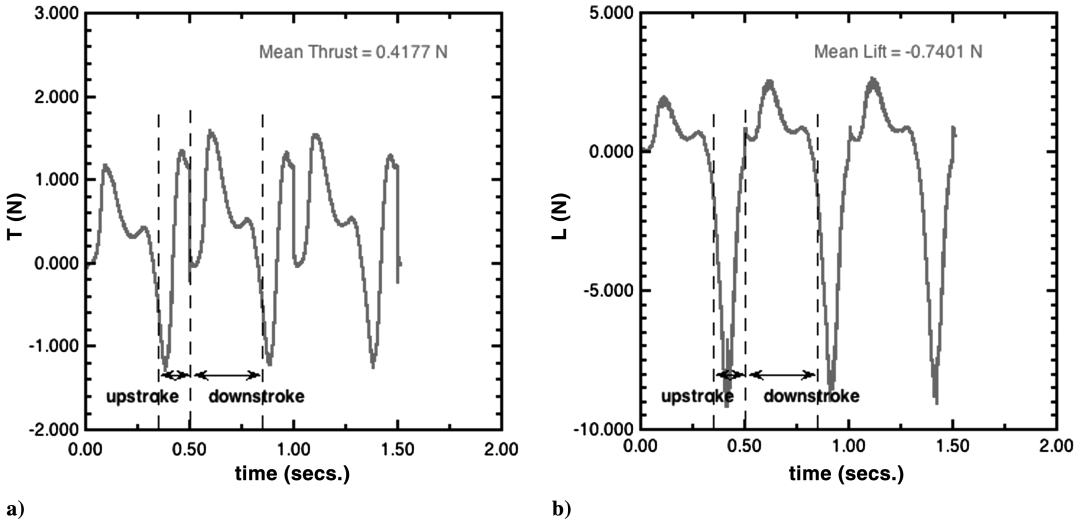

Fig. 27 Thrust and lift production on a hovering NRL-UUV with fins flapping at 2 Hz.

and the amplitude and frequency have to be taken into account, which is beyond the scope of this paper.

Identification of sets of kinematics that will yield positive lift forces is an important aspect of the design of a controller for steady level flight. One way to achieve the lift is to vary the flexibility of the fin as shown here, but this is accompanied by the loss of thrust. Another method to obtain mean positive lift is to change the starting location of the downstroke. In this study, three starting locations were considered. Simulations were performed by varying $\phi_0 = \{-85°, -65°, -45°\}$ for $k_b = \{1.25, \quad 1.5, \quad 1.75\}$ and $k_f = \{0.0, \quad 0.5, \quad 1.0, 1.5\}$. Figure 24 shows the mean thrust and lift generated as a function of the bulk amplitude, fin flexibility, and the starting location of the downstroke. For clarity of visualization, the surfaces corresponding to $\phi_0 = -85$ and $-45°$ are shifted by ± 0.1 N. As the fin flexibility is decreased, the mean lift increases almost linearly while the other two parameters are fixed. A similar effect is achieved by changing the starting location of the downstroke. The range of mean thrust and lift forces obtained by varying fin flexibility and downstroke starting location suggests that these are viable control parameters for vertical stability of the UUV.

F. Hydrodynamic Characteristics of NRL-UUV

A new test vehicle shown in Figs. 25a and 25b, has been designed (Palmisano et al. [16]), which carries a set of two actively controlled curvature fins in order to demonstrate thrust production and vertical plane controllability in an underwater test environment. The performance of a newly developed UUV under various swimming speeds [$V = 1$ kt (0.5144 m/s) and 2 kt (1.0289 m/s)] and pitch angle of attack [$\alpha = 0$ to 30° and side-slip angles ($\beta = 0$ to 15°)] was also mapped out. Figure 25c shows the pressure distribution on the vehicle at one of the flow conditions. Figure 26 shows the variation of coefficients of lift and drag and normal forces. The results of these simulations together with the characteristics of the flapping fin described in the previous section were incorporated into the controller development.

Figure 27 shows the force generated by the flapping fins on the hovering NRL-UUV. The surface pressure distribution on the vehicle at one instant during the flapping cycle is shown in Fig. 28. The drag

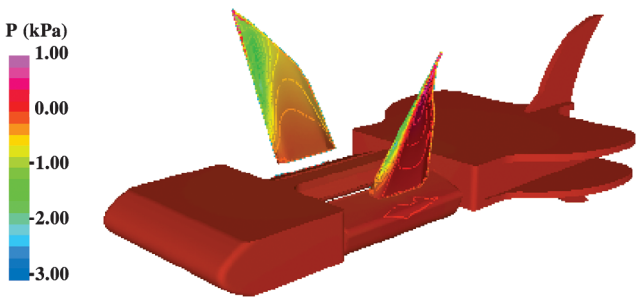

Fig. 28 Surface pressure distribution on a hovering NRL-UUV at $t = 1.09$ s.

force on the vehicle traveling at 1 kt is 0.25 N. It is clear that the mean thrust force is sufficient to propel the vehicle to more than 1 kt. However, the mean negative lift suggests that we need a vehicle controller that is capable of maintaining vertical position while still enabling this forward speed. Hence, the computed results from the parametric studies on the control variables were used in conjunction with the controller design and were successfully tested by Geder et al. [22] using three different control methods, both for vertical level flight and yaw motion.

IV. Conclusions

Three-dimensional, unsteady computations of an actively controlled-curvature flapping fin have been carried out. The computed results are validated against experimental data, and the comparison is good. Simulations were performed for flow past a fin test vehicle incorporating the flapping deforming fins. Several parameters controlling the kinematics of the fin were varied. The fin flapping at 2 Hz was able to provide mean positive thrust for a vehicle speed up to 2 kt. To achieve a controlled, steady level flight, it is necessary to have kinematics that would yield positive lift forces. Increasing the rigidity of the fin was found to result in mean positive lift, while the thrust generated decreased. Altering the mean stroke bias angle produced a similar effect. These two parameters have been computationally shown to provide a viable set of control parameters for steady level flight and yaw motion of the UUV. The hydrodynamic characteristics of a newly built prototype vehicle at NRL were computed for a range of operational conditions. The propulsion performance of the deforming fins has been computationally demonstrated to provide adequate force production and controllability for the fin test vehicle.

Acknowledgments

This work was supported by the Office of Naval Research (ONR) through an NRL 6.2 project: "Unsteady Hydrodynamics of Swimming Vehicles." This work was supported in part by a grant of high-performance computing (HPC) time from the U.S. Department of Defense (DoD) HPC Center at NRL. The authors would like to thank Rainald Löhner of George Mason University for his assistance throughout the course of this work.

References

[1] Blake, R. W., "The Mechanics of Labriform Motion 1: Labriform Locomotion in the Angelfish (*Pterophyllum eimekei*): An Analysis of the Power Stroke," *Journal of Experimental Biology*, Vol. 82, 1979, pp. 255–271.

[2] Platzer, M. F., and Jones, K. D., "Flapping Wing Aerodynamics—Progress and Challenges," AIAA Paper 2006-500, Jan. 2006.

[3] Rozhdestvensky, K. V., and Ryzhov, V. A., "Aerohydrodynamics of Flapping Wing Propulsors," *Progress in Aerospace Sciences*, Vol. 39, No. 8, 2003, pp. 585–633. doi:10.1016/S0376-0421(03)00077-0

[4] Shyy, W., Berg, M., and Ljungqvist, D., "Flapping and Flexible Wings for Biological and Micro Air Vehicles," *Progress in Aerospace Sciences*, Vol. 35, No. 5, 1999, pp. 455–505. doi:10.1016/S0376-0421(98)00016-5

[5] Kato, N., Liu, H., and Morikawa, H., "Biology-Inspired Precision Maneuvering of Underwater Vehicles," *Proceedings of the 12th International Journal of Offshore and Polar Engineering Conference*, Vol. 2, 2002, pp. 269–276.

[6] Ando, Y., Kato, N., Suzuki, H., Ariyoshi, T., Suzumori, K., Kanda, T., and Endo, S., "Elastic Pectoral Fin Actuators for Biomimetic Underwater Vehicles," *Proceedings of the 16th International Offshore and Polar Engineering Conference*, 2006, pp. 260–267.

[7] Tangorra, J. L., Davidson, S. N., Hunter, I., Madden, P. G. A., Lauder, G. V., Dong, H., Bozukurttas, M., and Mittal, R., "The Development of a Biologically Inspired Propulsor for Unmanned Underwater Vehicles," *IEEE Journal of Oceanic Engineering*, Vol. 32, No. 3, July 2007, pp. 533–550. doi:10.1109/JOE.2007.903362

[8] Walker, J. A., and Westneat, M. W., "Labriform Propulsion in Fishes: Kinematics of Flapping Aquatic Flight in the Bird Wrasse, *Gomphosus Varius* (Labridae)," *Journal of Experimental Biology*, Vol. 200, No. 11, 1997, pp. 1549–1569.

[9] Ramamurti, R., Sandberg, W. C., Löhner, R., Walker, J. A., and Westneat, M. W., "Fluid Dynamics of Flapping Aquatic Flight in the Bird Wrasse: 3-D Unsteady Computations with Fin Deformation," *Journal of Experimental Biology*, Vol. 205, No. 19, Oct. 2002, pp. 2997–3008.

[10] Palmisano, J., Geder, J., Ramamurti, R., Liu, K. J., Cohen, J., Mengesha, T., Naciri, J., Sandberg, W. C., and Ratna, B., "Design, Development and Testing of Flapping Fins with Actively Controlled Curvature for an Unmanned Underwater Vehicle," *Bio-Mechanisms of Swimming and Flying*, edited by N. Kato and S. Kamimura, Springer, New York, 2007, pp. 283–294.

[11] Ramamurti, R., and Löhner, R., "Evaluation of an Incompressible Flow Solver Based on Simple Elements," *Advances in Finite Element Analysis in Fluid Dynamics*, Fluids Engineering Div. 137, American Society of Mechanical Engineers, New York, 1992, pp. 33–42.

[12] Ramamurti, R., Löhner, R., and Sandberg, W. C., "Computation of the 3-D Unsteady Flow Past Deforming Geometries," *International Journal of Computational Fluid Dynamics*, Vol. 13, No. 1, 1999, pp. 83–99. doi:10.1080/10618569908940891

[13] Ramamurti, R., and Sandberg, W. C., "Computational Fluid Dynamics Study for Optimization of a Fin Design," 24th AIAA Applied Aerodynamics Conference, AIAA Paper 2006-3658, San Francisco, 2006.

[14] Ramamurti, R., Sandberg, W. C., and Löhner, R., "The Influence of Fin Rigidity and Gusts on the Force Production in Fishes and Insects: A Computational Study," AIAA Paper 2004-0404, Washington, D.C., Jan. 2004.

[15] Trease, B. P., Lu, K. J., and Kota, S., "Biomimetic Compliant System for Smart Actuator-Driven Aquatic Propulsion: Preliminary Results," ASME International Mechanical Engineering Congress & Exposition, Washington, D.C., American Society of Mechanical Engineers Paper IMEC2003-41446, 2003.

[16] Palmisano, J., Geder, J., Ramamurti, R., Sandberg, W. C., and Ratna, B., "Real-Time Robotic Pectoral Fin CPG Using Weighted Gait Combinations," *IEEE Transactions on Robotics and Automation* (submitted for publication).

[17] Geder, J., Sandberg, W. C., and Ramamurti, R., "Multi-Camera, High-Speed Imaging System for Kinematics Data Collection," Naval Research Lab, Washington, D.C., Rept. NRL/MR/6401-07-9054, Sept. 2007.

[18] Bohl, D. G., and Koochesfahani, M. M., "MTV Measurements of the Vortical Field in the Wake of an Airfoil Oscillating at High Reduced Frequency," *Journal of Fluid Mechanics*, Vol. 620, No. 1, 2009, pp. 63–88. doi:10.1017/S0022112008004734

[19] Ramamurti, R., and Sandberg, W. C., " Simulation of Flow About Flapping Airfoils Using Finite Element Incompressible Flow Solver," *AIAA Journal*, Vol. 39, No. 2, 2001, pp. 253–260. doi:10.2514/2.1320

[20] Smagorinsky, J., "General Circulation Experiments with the Primitive Equations. 1. The Basic Experiment," *Monthly Weather Review*, Vol. 91, 1963, pp. 99–164. doi:10.1175/1520-0493(1963)091<0099:GCEWTP>2.3.CO;2

[21] Ramamurti, R., and Sandberg, W. C., "A Three-Dimensional Computational Study of the Aerodynamic Mechanisms of Insect Flight," *Journal of Experimental Biology*, Vol. 205, No. 10, 2002, 1507–1518.

[22] Geder, J., Palmisano, J., Ramamurti, R., Sandberg, W. C., and Ratna, B., "Fuzzy Logic PID Based Control Design and Performance for a Pectoral Fin Propelled Unmanned Underwater Vehicle," *Proceedings of the International Conference on Control, Automation and Systems*, Seoul, ROK, Oct. 2008.

K. Willcox
Associate Editor